

## Chapter 2

# Synthesis and In-house Characterization of Materials

### 2.1 Synthesis

#### 2.1.1 Nanoparticles

ZnO nanoparticles (NPs) were synthesized through a sol-gel method in collaboration with Dr. Noemi Carmona, at the Complutense University of Madrid.

The sol-gel method has gained notoriety in the glass and ceramic fields. Indeed, it has grown to be so important that in the 1990s more than 35,000 papers were published worldwide on the process [1–4]. This method is a cheap and low-temperature technique that allows for the fine control of the product's chemical composition. Inorganic oxide materials with desirable properties of hardness, optical transparency, chemical durability, tailored porosity, and thermal resistance, can be produced at room temperatures, as opposed to the much higher melting temperatures required in the production of conventional inorganic glasses [2]. Even small quantities of dopants, such as organic dyes and rare earth elements, can be introduced in the sol and end up uniformly dispersed in the final product.

The applications for sol gel-derived products are numerous, and derived from the various material shapes generated in the gel state (aerogels, monolith ceramics, glasses, films, fibers, and monosized powders such as nanospheres). Among the aforesaid applications are included protective and porous films, optical coatings, window insulators, dielectric and electronic coatings, high temperature superconductors, reinforcement fibres, fillers, and catalysts, (bio)sensors, medicine applications (e.g., controlled drug release), reactive material and separation (chromatography) technology.

Three reactions are generally used to describe the sol-gel process: hydrolysis, alcohol condensation and water condensation. The 'sol' (solution) evolves towards the formation of a gel-like diphasic system containing both a liquid and a solid phase whose morphologies range from discrete particles to continuous polymer networks.

Typical precursors are metal alkoxides and metal chlorides, which undergo hydrolysis and polycondensation reactions to form a colloid. The basic structure or morphology of the solid phase can range anywhere from discrete colloidal particles to continuous chain-like polymer networks [5]. In the case of colloid, the volume fraction of particles (or particle density) may be so low that a significant amount of fluid may need to be removed initially for the gel-like properties to be recognized. The simplest method to accomplish that is to allow time for sedimentation to occur, and then pour off the remaining liquid. Removal of the remaining liquid (solvent) phase requires a drying process, which is typically accompanied by a significant amount of shrinkage. In principle, the ultimate structure of the final component would be strongly influenced by changes imposed upon the structural template during this phase of processing. However, the characteristics and properties of a particular sol-gel inorganic network are related to a number of factors that affect the rate of hydrolysis and condensation reactions [6], such as pH, temperature and time of reaction, reagent concentrations, catalyst nature and concentration, molar ratios, ageing temperature and time. Thus, by controlling these factors, it is possible to vary the structure and properties of the sol-gel-derived inorganic network over wide ranges [7]. In addition, the degree of order appears to be limited by the time and space allowed for longer-range correlations to be established, and so, defective polycrystalline structures would appear to be the basic elements of nanoscale materials science [8].

For the synthesis of our NPs, dimethyl sulfoxide (DMSO,  $(\text{CH}_3)_2\text{SO}$ , 99.9 %, Sigma Aldrich) and absolute ethanol ( $\text{CH}_3\text{CH}_2\text{OH}$ , 99.95 %, Panreac) were used as solvents; zinc acetate dihydrate ( $\text{Zn}(\text{CH}_3\text{CO}_2)_2 \cdot 2\text{H}_2\text{O}$ , 98 %, Sigma Aldrich) as precursor; tetramethylammonium hydroxide pentahydrate (TMAH,  $\text{N}(\text{CH}_3)_4\text{OH}$ , 97 %, Sigma Aldrich) to perform the hydrolysis and trioctylphosphine (hereafter TOPO), dodecylamine (hereafter AMINE), and dodecanethiol ( $\text{CH}_3(\text{CH}_2)_{11}\text{SH}$ , 98 %, Sigma Aldrich) as capping agents.

5 mmol of zinc acetate was dissolved with continuous stirring in DMSO and the solution was kept at 60 °C. Then, a 7.5 mmol solution of TMAH in ethanol at 60 °C was dropped to the previous one. After  $t_{\text{add}}$  min stirring, where  $t_{\text{add}}$  is the time waited once the synthesis was initiated, a 7.5 mmol solution of the capping agent was added all at once. Since the capping molecule should stop the growth of the NPs, the idea of varying  $t_{\text{add}}$  is to get NPs of different sizes, being supposedly bigger as  $t_{\text{add}}$  is increased. The obtained ZnO NPs that precipitated were filtrated and washed using absolute ethanol at 60 °C to remove unreacted precursors, and the washing process was repeated three times. The purified NPs were then left to dry in air for 2 days.

The samples, listed in Table 2.1, were prepared in several series (labelled from 1 to 5), each series using identical starting solution. The first synthesis was made by adding the capping agent 20 min after the addition of the TMAH. Part of the samples were placed inside a petri-dish and submitted to a thermal treatment at 350 °C in a muffle furnace for 1 h (heating time from 20 to 350 °C was 1 h and cooling process took another hour). This process removes the organic part of the samples. We refer to these samples as calcinated. In the second batch of samples only dodecanethiol was used as capping agent and  $t_{\text{add}}$  was varied between 0 and 30 min in order to prepare ZnO NPs of different sizes, being  $t_{\text{add}} = 5$  min (hereafter

**Table 2.1** List of the ZnO NPs synthesized through sol-gel method in this work

Sample	Capping agent	$t_{add}$ (min)
TOPO	Trioctylphosphine	20
AMINE	Dodecylamine	20
20-12C-1 (THIOL)	Dodecanethiol	20
20-12C-1-Calc	Dodecanethiol	20
5-12C-2	Dodecanethiol	5
15-12C-2	Dodecanethiol	15
30-12C-2	Dodecanethiol	30
7-12C-3	Dodecanethiol	7
9-12C-3	Dodecanethiol	9
12-12C-3	Dodecanethiol	12
20-4C-4	Butanethiol	20
20-8C-4	Octanethiol	20
20-12C-4	Dodecanethiol	20
30-4C-4	Butanethiol	30
30-8C-4	Octanethiol	30
30-12C-4	Dodecanethiol	30
40-4C-4	Butanethiol	40
40-8C-4	Octanethiol	40
40-12C-4	Dodecanethiol	40
50-4C-4	Butanethiol	50
50-8C-4	Octanethiol	50
50-12C-4	Dodecanethiol	50
TOPO-5	Trioctylphosphine	20
AMINE-5	Dodecylamine	20
20-12C-5 (THIOL-5)	Dodecanethiol	20

5-12C-2 sample), 15 min (15-12C-2), and 30 min (30-12C-2). Similarly, in a third series the samples 7-12C-3, 9-12C-3, 12-12C-3 were synthesized. To study the influence of the length of the carbon chains into the magnetic properties of the NPs, a new series of samples were prepared by using different capping organic molecules: butanethiol ( $\text{CH}_3\text{CH}_2\text{CH}(\text{SH})\text{CH}_3$ , 98 %, Sigma Aldrich) (4 carbon atoms in the organic chain, referred as  $t_{add}$ -4C-4), octanethiol ( $\text{CH}_3(\text{CH}_2)_7\text{SH}$ , 98.5 %, Sigma Aldrich) (8 carbon atoms,  $t_{add}$ -8C-4) and dodecanethiol (12 carbon atoms,  $t_{add}$ -12C-4). Additionally, a final series was prepared by repeating the parameters (capping and  $t_{add}$ ) of the first one.

It has to be mentioned at this point that among the main drawbacks of the preparation of NPs stand out the reproducibility of each synthesis and the stability of the NPs once prepared. It is well known that the reaction yield in the preparation of the NPs is low, and so the same process is typically repeated several times until enough

sample amount is obtained. Synthesis reproducibility has been tested by performing X-ray diffraction (XRD) and X-ray Absorption Spectroscopy (XAS) analysis. Major differences are observed between nominally identical samples from different batches indicating the low reproducibility of the synthesis method. As a consequence, in this study samples synthesized in the same way but from different batches are clearly labelled as different samples (e.g. 20-12C-1 and 20-12C-4). This implies that the whole characterization of the samples has been carried out for each specimen. On the other hand, the stability of the as synthesized ZnO NPs has been proved by overlapping of successive XAS spectra recorded during the 3 years period on the same samples and specimens. No modification of the absorption spectra has been found on the same specimens measured at the initial run and upto 3 years later, either in different specimens prepared from the same sample. As it will be discussed in the next chapters, this indicates that the observed properties are intrinsic and stable in time.

### ***2.1.2 Thin Films and Multilayers***

ZnO/ZnS multilayers were prepared by RF-sputtering in collaboration with Dr. Eva Céspedes at the Institute of Materials Science of Madrid (ICMM). The specific equipment used consists of a PLS 500 Pfeiffer high vacuum system equipped with a TMH 520 turbomolecular pump. Details of this equipment can be found elsewhere [9].

The sputtering deposition method [10–14] is a physical vapour deposition process in which a bulk starting material (target) is eroded by a particle bombardment and subsequently deposited onto a substrate. The process is presented in Fig. 2.1 in its simplest form: a target material is placed in a vacuum chamber filled with a gas at a reduced pressure and a negative potential, that accelerates the electrons present in the process chamber towards the grounded chamber wall, is set on. The electrons collide with gas molecules and generate electron-ion pairs. The ions from the electron-ion pairs are accelerated towards the target (cathode) and upon impact with the target surface two events take place: (i) an atomic collision cascade in which some of the target material can be ejected and condense onto the surrounding surfaces, and (ii) a number of secondary emitted electrons are accelerated and ionize the gas molecules. The described cathodic process is also called DC sputtering. A disadvantage of the diode sputtering is that the deposition rate is slow and the electron bombardment of the substrate is extensive, what can cause overheating and structural damage. However, those problems are solved by the use of magnetron sputtering, i.e. by using magnets behind the cathode to trap the free electrons in a magnetic field directly above the target surface. These electrons are not free to bombard the substrate to the same extent as in diode sputtering. At the same time the circular path carved by these same electrons when trapped in the magnetic field, enhances their probability of ionizing a neutral gas molecule by several orders of magnitude. This rise in available ions significantly increases the rate at which target material is eroded and subsequently deposited onto the substrate. In addition, a problem of DC sputtering is that the target must be a conducting material to avoid charging.

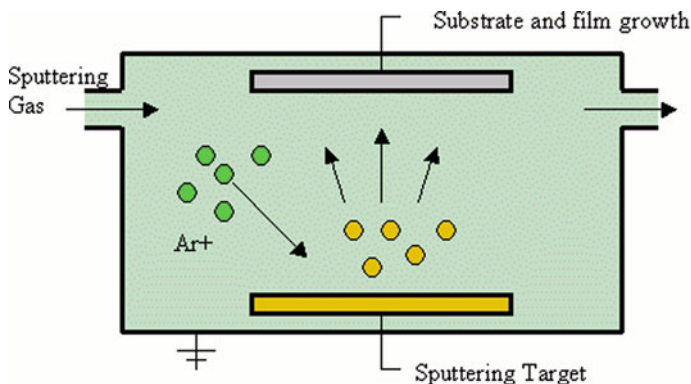


**Fig. 2.1** Schematized sputtering process. Positive ions from a gas discharge are accelerated towards a target and create upon impact: (i) an atomic collision cascade in which some of the target material can be ejected and condense onto the surrounding surfaces, and (ii) a number of secondary emitted electrons which are then accelerated and ionize the gas molecules

If an isolating target material is set on a negative potential the ion collisions will charge up the surface of the target, resulting in an electrical breakdown in the form of arcing. This can be avoided with the use of radio frequency (RF) sputtering. In this mode of sputtering, the sign of the anode-cathode bias is varied at a high rate (the Federal Communications Commission has reserved a frequency of 13.56 MHz for the plasma processing techniques and so is the most widely used [15]). Since electrons are lighter, they follow better the changes in the AC electric field. Hence, a large electron current is drawn at the target followed by a small positive ion current, making the net current flow different from zero over the complete period of one cycle. Thus, the target self-biases to a negative potential to avoid a net current through the capacitor. A combination of capacitors and inductors is used to form an impedance matching network which maximizes the power delivery by forming an effective coupling of the RF power supply and the target. The impedances of materials with high resistivity that cannot be DC sputtered drop with increasing frequency and so, high frequencies pass current through dielectric targets.

In this work, ZnO/ZnS multilayers were prepared by RF-sputtering on fused silica substrates at room temperature by alternative sputtering from ZnO and ZnS two-inch ceramic targets. Residual chamber pressure was in the  $10^{-7}$  mbar range. Both ZnO and ZnS layers were prepared using Ar at  $5.1 \times 10^{-3}$  mbar and 20 W. Growth rates, measured by X-ray reflectivity, were about 1.5 and 3.5 nm/min for ZnO and ZnS, respectively. Deposition started with ZnO and a last additional ZnO 4 nm layer was deposited on top. Following this procedure, two samples labelled  $(\text{ZnO}_{4\text{nm}}/\text{ZnS}_{4\text{nm}})_{10}$  (+ZnO 4 nm) and  $(\text{ZnO}_{2\text{nm}}/\text{ZnS}_{2\text{nm}})_{20}$  (+ZnO 4 nm) were prepared, keeping constant the ZnO and ZnS total thickness and modifying the number of interfaces.

In addition, a Zn-O-S thin film (ZnS/ZnO 50%/50%) was prepared by RF co-sputtering from ZnO and ZnS two-inch ceramic targets placed at  $15^\circ$ . The sample

was grown using Ar gas (9.1 sccm), on Si(100) and quartz substrates at room temperature. The base pressure provided by the vacuum system was  $1 \times 10^{-6}$  mbar and the working pressure was  $5.2 \times 10^{-3}$  mbar. The RF power supplied was about 20 W for ZnS and 30 W for ZnO. Under these conditions, the growth rate is nominally the same for both targets and the samples were grown for 24 min, corresponding to a nominal 100 nm thickness, in agreement with X-ray reflectivity data (see Sect. 2.2.2). A part of the co-sputtered samples was annealed in a quartz tube placed inside a furnace and under an O<sub>2</sub> controlled flow (5 sccm,  $5.0 \times 10^{-3}$  mbar pressure).

## 2.2 Structural Characterization

### 2.2.1 X-ray Diffraction (XRD)

X-ray diffraction (XRD) measurements were performed in a Bruker D8 fast X-ray diffractometer (Lynxeye) from the ICMC diffraction service, in collaboration with Dr. Eva Céspedes, Dr. Ana Espinosa and Dr. M. Ángeles Laguna-Marco.

The XRD patterns of the AMINE, TOPO and THIOL NPs (first series) are shown in Fig. 2.2. The patterns were indexed on the basis of a ZnO wurtzite (W-ZnO) type unit cell. The particle size ( $D_{XRD}$ ) has been calculated by measuring the full width at half maximal (FWHM) intensity of three Bragg diffraction peaks, centred at  $2\theta = 31.1^\circ$ ,  $34.3^\circ$  and  $36.2^\circ$ , those correspond to the (100), (002) and (101) reflection from the wurtzite structure. For obtaining the values of the FWHM, each peak was fitted by a Gaussian or Lorentzian curve (see Fig. 2.3). Then, we averaged the values obtained by using the Scherrer formula for each peak:

**Fig. 2.2** X-ray diffraction patterns of **a** the bulk ZnO and ZnS references and **b** the series-1 of ZnO NPs capped with organic molecules (TOPO, AMINE and THIOL)

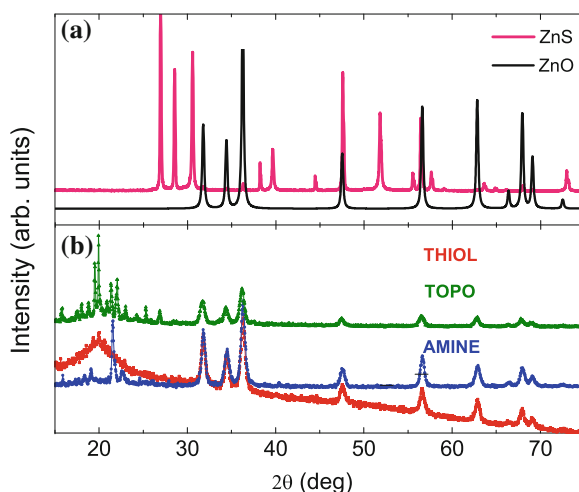
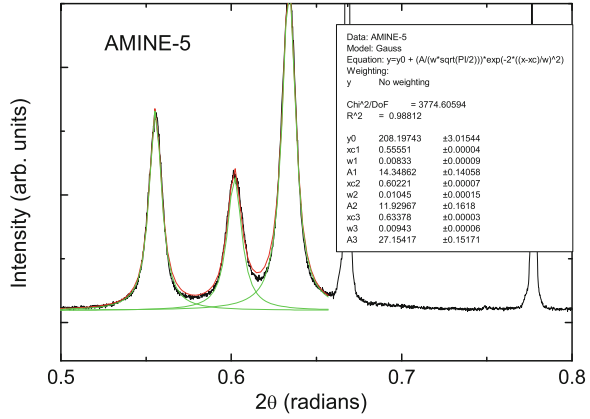


**Fig. 2.3** Standard procedure to calculate the crystal grain size ( $D_{XRD}$ ) of the NPs. In the case of AMINE-5 the peaks are fit by Gaussian curves. The peaks position and FWHM are obtained from the fit and introduced in the Scherrer formula (see text)



$$l = \frac{K \cdot \lambda}{B \cos \theta} \quad (2.1)$$

where  $l$  is the crystallite size,  $\lambda$  is the wavelength of the X-ray radiation used (in our case the Cu  $K_{\alpha}$ , that is, 1.5418 Å),  $B$  is the peak width (radians) due to particle size effect, and  $\theta$  is the Bragg angle. The numerical factor  $K$  depends on the crystal shape and the definitions of the average crystallite size (for example, if the cube root of the crystallite volume is used instead of the definition above) and the width (for example, if the integral line width is used, rather than the FWHM). In the absence of detailed shape information  $K = 0.9$  is a good approximation, hence we adopted this value. The results of our analysis are summarized in the Table 2.2.

The XRD patterns show also the presence of an amorphous phase and low angle peaks coexisting with the crystalline W-ZnO like. Similar behaviour is found in the ZnO NPs obtained in different batches, the main difference being the amount ratio of the amorphous and the crystalline phases. This is exemplified in Figs. 2.4 and 2.5, where representative XRD patterns of samples of series-2, -4 and -5 are shown.

As shown in these figures the crystallinity of the samples and the amount of the amorphous phases strongly depend on the synthesis conditions. However no relationship can be established with any of the parameters varied through the synthesis process. In addition, in some of the samples the amorphous phase is dominant, which prevents us from applying the Scherrer formula to determine the particle size.

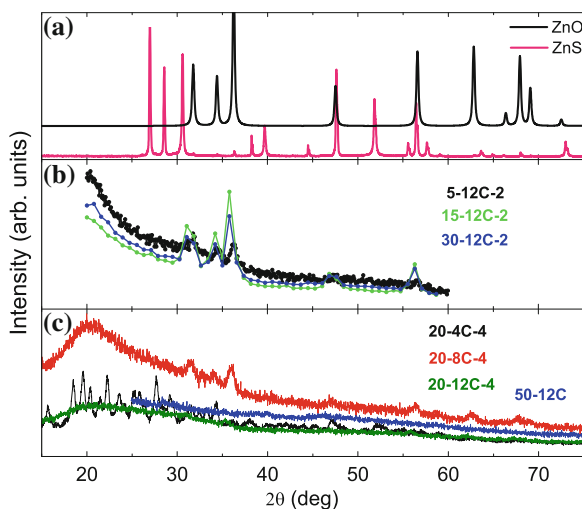
In principle, the existence of an amorphous phase and low angle peaks could be addressed to the organic part of the material. In order to verify this possibility some of the samples were subjected to a calcination process aimed to remove the organic part of the material. This is shown in Fig. 2.6 where the thermal gravimetric analysis (TGA) in the case of AMINE is reported.

However the result of the calcination is not so satisfactory. Despite the original amorphous component disappears, there is an unexpected broadening of the X-ray

**Table 2.2**  $D_{XRD}$  of capped ZnO NPs

Sample	$D_{XRD}$ (nm)
AMINE	$18 \pm 2$
TOPO	$15 \pm 2$
20-12C-1 (THIOL)	$14 \pm 2$
20-12C-1 calcinated	$15 \pm 2$
5-12C-2	$13 \pm 2$
15-12C-2	$10 \pm 2$
30-12C-2	$12 \pm 2$
20-8C-4	$8 \pm 2$
20-12C-4	$8 \pm 2$
50-4C-4	$14 \pm 2$
50-8C-4	$8 \pm 2$
AMINE-5	$16 \pm 2$
TOPO-5	$13 \pm 2$
20-12C-5 (THIOL-5)	$10 \pm 2$

**Fig. 2.4** X-ray diffraction patterns of **a** the bulk ZnO and ZnS references, **b** the series-2 of ZnO NPs (5-12C-2, 15-12C-2 and 30-12C-2) and **c** representative NPs of the series-4 (20-4C-4, 20-8C-4, 20-12C-4 and 50-12C-4)



diffraction peaks. This is clearly illustrated in Fig. 2.7 where the XRD patterns of the 20-12C-1 sample prior and after calcination are shown. After calcination the XRD pattern indicates the occurrence of a ZnS phase. The peaks associated to the W-ZnO remain unaffected, but the ZnS phase appears highly disordered. This suggests that, in case of the ZnS phase being at the surface of the NPs, surrounding a ZnO core, the interface between the ZnO and ZnS phases would not be a pristine one, so that interpenetration of phases can not be ruled out.



**Fig. 2.5** X-ray diffraction patterns of **a** the bulk ZnO and ZnS references, **b** the series-5 of ZnO NPs capped with organic molecules (TOPO, AMINE and THIOL)

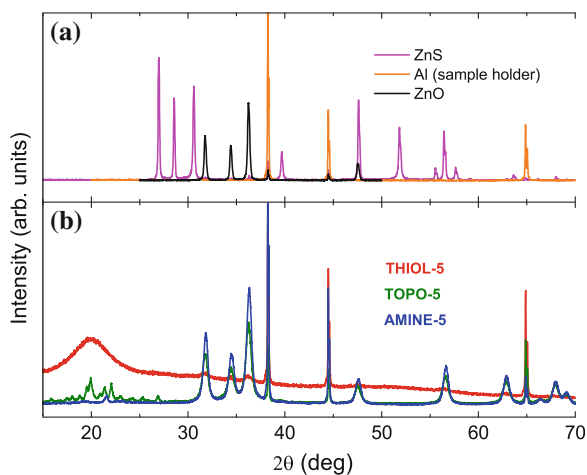


**Fig. 2.6** Thermal gravimetric treatment of the AMINE sample

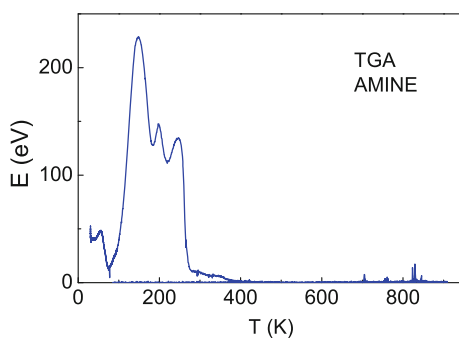
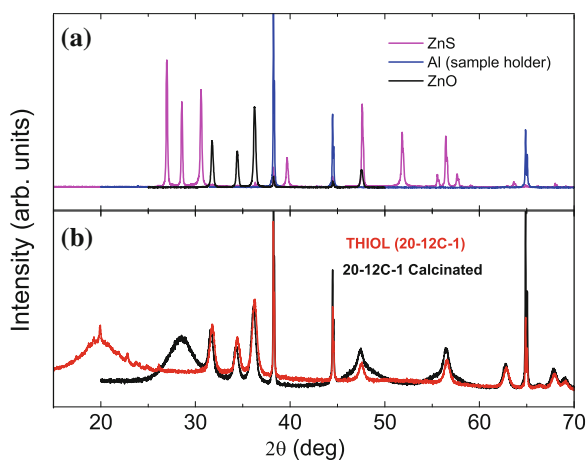


**Fig. 2.7** X-ray diffraction patterns of **a** the bulk ZnO and ZnS references, **b** 20-12C-1 sample prior and after calcination



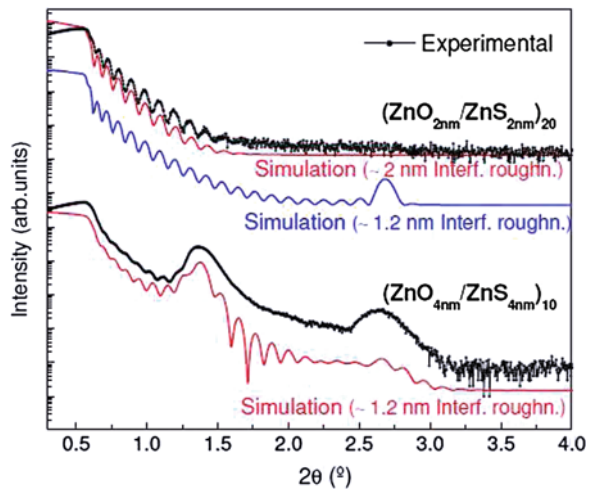
These results are also consistent with those found in the case of ZnO/ZnS multilayers (not shown) and the lack of diffraction peaks, even after annealing, in the case of the sample obtained by co-sputtering, indicating its high degree of structural disorder.

### 2.2.2 X-ray Reflectivity (XRR)

X-ray Reflectivity (XRR) measurements of the thin-film samples, were made in collaboration with Dr. Eva Céspedes at the ICMC by using a Bruker D8 X-ray diffractometer and Cu  $K_\alpha$  radiation.

The X-ray reflectivity spectra of both films are shown in Fig. 2.8, where Kiessig fringes, related to the total multilayers thickness, appear for both samples. Satellite maxima, associated with the bilayer period, are observed only for  $(\text{ZnO}_{4\text{nm}}/\text{ZnS}_{4\text{nm}})_{10}$  (+ZnO 4 nm) film, pointing to smoother ZnO/ZnS interfaces than for the  $(\text{ZnO}_{2\text{nm}}/\text{ZnS}_{2\text{nm}})_{20}$  one. The existence of flatter ZnO/ZnS interfaces in the  $(\text{ZnO}_{4\text{nm}}/\text{ZnS}_{4\text{nm}})_{10}$  (+ZnO 4 nm) sample is confirmed by XRR simulations performed by means of Xreal software (developed by Dr. Neil Telling [16]). Despite complex fits are away from the aim of this work these simulations, that mostly reproduce the shape of the experimental data, indicate a larger mean interface roughness for sample  $(\text{ZnO}_{2\text{nm}}/\text{ZnS}_{2\text{nm}})_{20}$  and what is more important, an average interface roughness of the order of the layer thickness, i.e., around 2 nm. That points towards differences in the morphology of both multilayers, laying  $(\text{ZnO}_{2\text{nm}}/\text{ZnS}_{2\text{nm}})_{20}$  in the regime between continuous and non-continuous layers, leading to more disordered ZnO/ZnS interfaces. This subject will center a deeper XAS study in the next chapters.

**Fig. 2.8** XRR reflectivity spectra of  $(\text{ZnO}_{4\text{nm}}/\text{ZnS}_{4\text{nm}})_{10}$  and  $(\text{ZnO}_{2\text{nm}}/\text{ZnS}_{2\text{nm}})_{20}$  multilayers and their simulations (see text for details)



### 2.2.3 Transmission Electron Microscopy (TEM), High Resolution Transmission Electron Microscopy (HRTEM) and Energy Dispersive X-ray Spectroscopy (EDX)

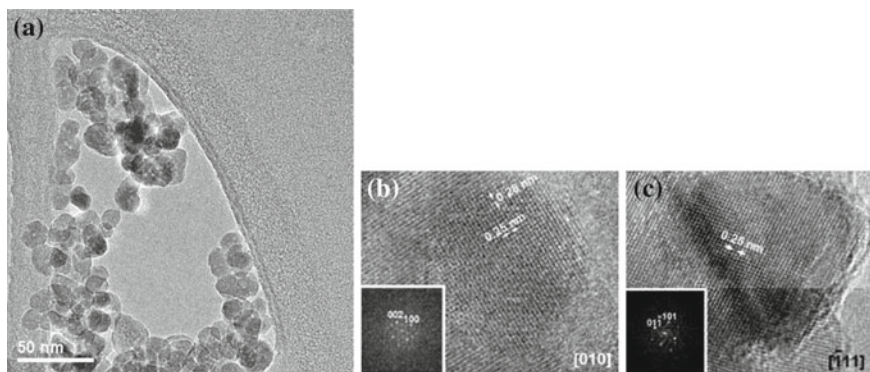
TEM, HRTEM and EDX measurements were undertaken by Dr. M. L. Ruíz-González and Dr. J. González-Calbet at the Complutense University of Madrid. A 200 kV JEOL2000FX transmission electron microscope and a JEOL3000FEG electron microscope fitted with an Oxford LINK EDX analyser were used.

Figure 2.9 shows the results obtained in the case of samples of series-1. Panel (a) of this figure shows a representative low magnification image of the TOPO sample evidencing an average size of 15–20 nm, in agreement with XRD data. HRTEM images and corresponding FT are shown in panels (b) and (c). They allow to distinguish interplanar distances of 2.5 nm, in agreement with the formation of wurtzite ZnO NPs.

Representative HRTEM images of the samples of the second series of synthesis are shown in Figs. 2.10, 2.11 and 2.12. The images indicate the low crystallinity of the samples although some NPs are clearly visible. This result is in agreement with the XRD data, indicating that the degree of crystallinity of the NPs strongly depends on the synthesis batch.

Finally, energy dispersive X-ray analysis (EDX) excludes the presence of magnetic impurities within the sensitivity (0.01 %) of this technique. In addition the EDX analysis provides an estimate of the ratio of the Zn versus S content in both the crystalline and amorphous phases. The fact that Zn is also present in the amorphous phase indicates that it is not due to the organic part of the capping molecules but to low crystallinity regions of the NPs.

In the case of multilayers, cross-sectional TEM images are shown in Fig. 2.13 for both  $\text{ZnO}_{4\text{nm}}/\text{ZnS}_{4\text{nm}}$  and  $\text{ZnO}_{2\text{nm}}/\text{ZnS}_{2\text{nm}}$  samples. According to the expected



**Fig. 2.9** Low magnification (a) and HRTEM (b, c) images, including their corresponding FT, of the TOPO sample

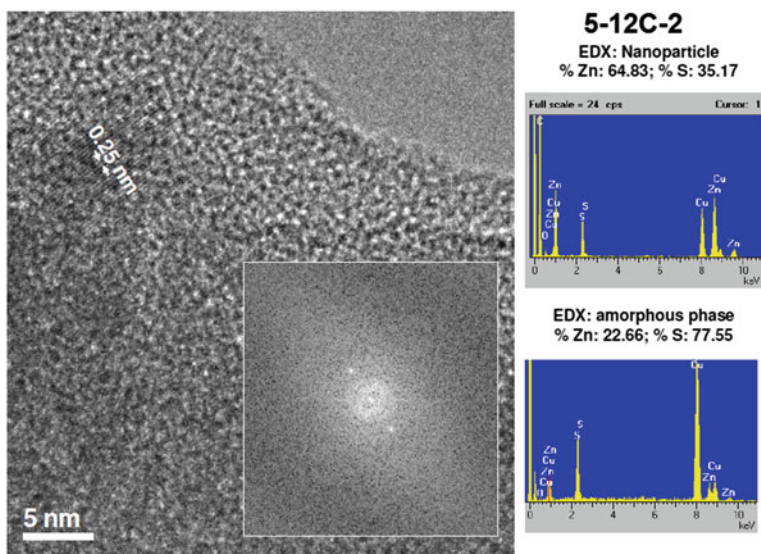


**Fig. 2.10** HRTEM and EDX of the 5-12C-2 sample

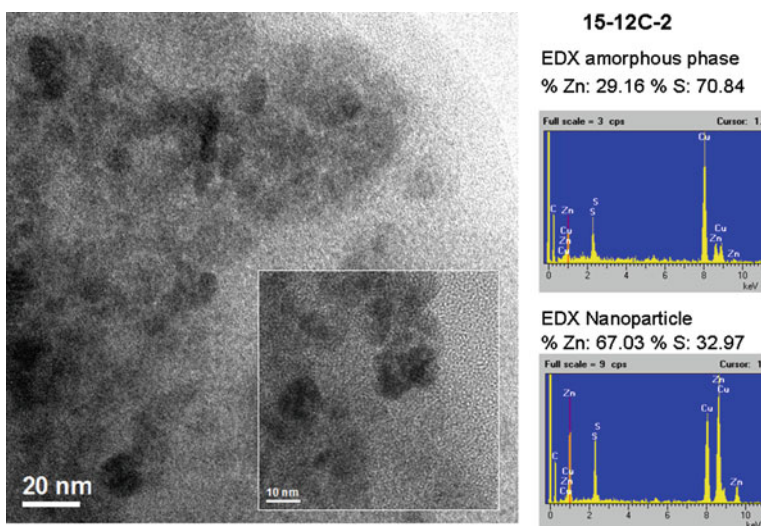


**Fig. 2.11** HRTEM and EDX of the 15-12C-2 sample

values, layer thickness of  $4 \pm 1$  and  $2 \pm 1$  nm are obtained from TEM for each ZnO and ZnS layer forming the  $(\text{ZnO}_{4\text{nm}}/\text{ZnS}_{4\text{nm}})_{10}$  and  $(\text{ZnO}_{2\text{nm}}/\text{ZnS}_{2\text{nm}})_{20}$  samples, respectively. Despite heterostructure periodicity is distinguished for both samples, TEM insets of Fig. 2.13 confirm the presence of more disorder ZnO/ZnS regions coexisting in the  $(\text{ZnO}_{2\text{nm}}/\text{ZnS}_{2\text{nm}})_{20}$  sample.

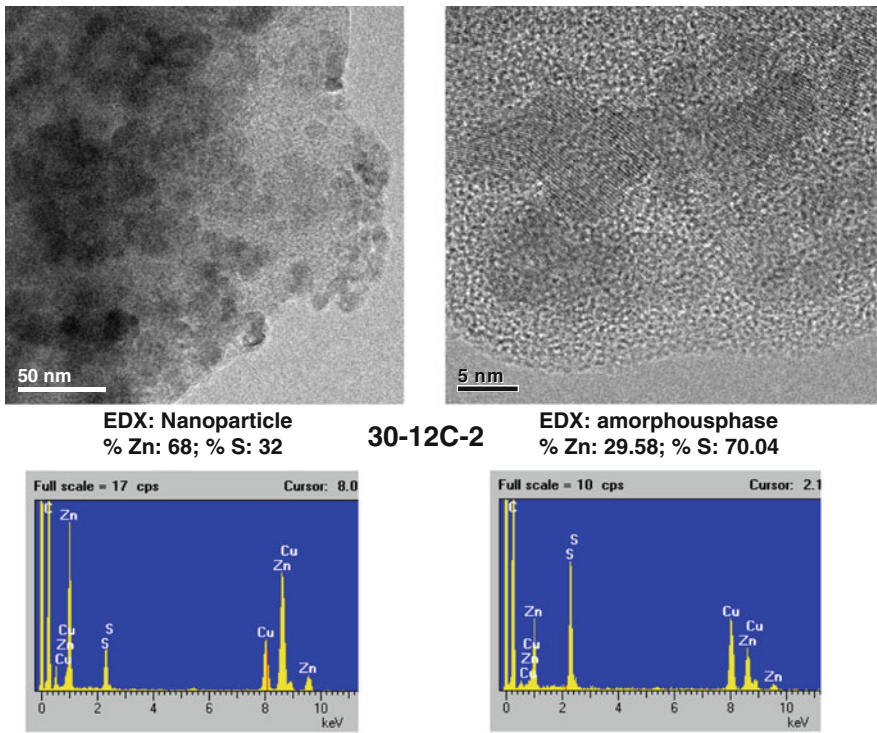


Fig. 2.12 HRTEM and EDX of the 30-12C-2 sample

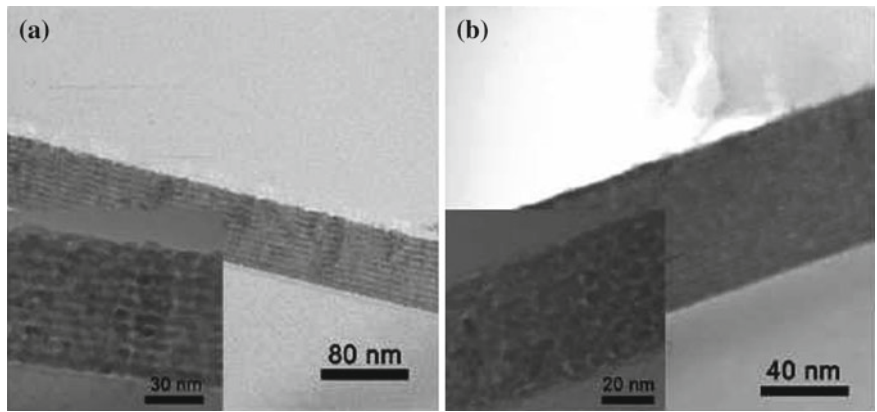


Fig. 2.13 Cross-sectional TEM images of **a**  $(\text{ZnO}_{4\text{nm}}/\text{ZnS}_{4\text{nm}})_{10}$  and **b**  $(\text{ZnO}_{2\text{nm}}/\text{ZnS}_{2\text{nm}})_{20}$  multilayers

## 2.3 Optical Absorption

Optical absorption and luminescence studies were conducted in collaboration with Dr. M.A. García and the Institute of Ceramic and Glass (ICV). Some of the measurements are previous to the development of this PhD work [17] but they have been included here for the sake of completeness.

Photoluminescence (PL) excitation and emission spectra were recorded with a Perkin-Elmer LS-5 spectrofluorometer performing the appropriate correction for the lamp intensity and photomultiplier spectral response. Powder samples were placed in a circular sample holder and covered with a quartz window. No significant contribution from the sample holder or from the quartz window to the emission or excitation bands in the spectral region of interest was found. Reflectance was measured with a Shimadzu 3100 monochromator with an integrating sphere attached to collect both specular and diffuse reflectance using the same sample holder than for the PL measurements. No significant contribution of the sample holder nor from the window was found.

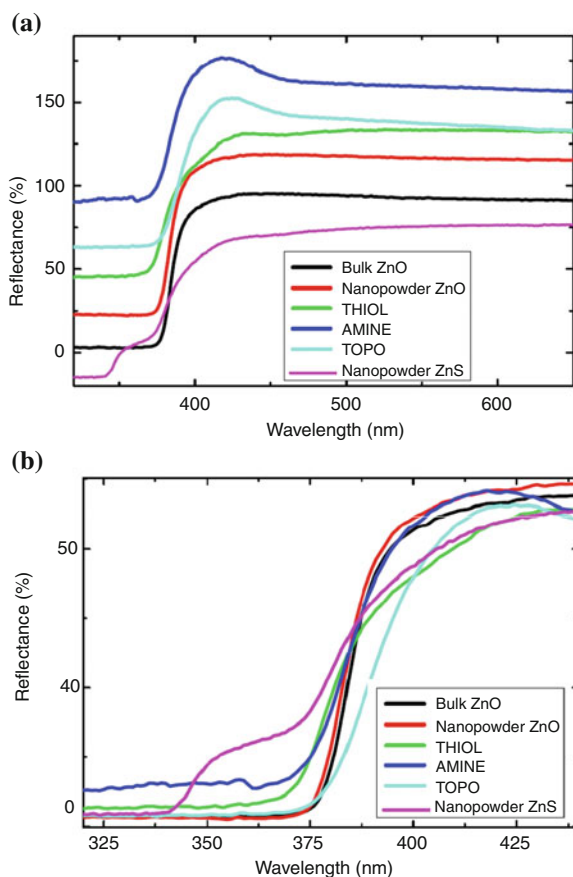
As ZnO is a degenerated semiconductor with an energy gap (3.35 eV) in the UV-Vis part of the spectrum, optical spectroscopy probing transitions between valence and conduction band provides useful information about its electronic structure. Figure 2.14 shows the integrated reflectance of the samples in the 350–650 nm range. Bulk ZnO exhibits a typical plain profile at the visible part of the spectrum with a sharp decay at  $\sim 400$  nm reflecting the ZnO bandgap. A reference sample of ZnO nanopowder (particle size  $\sim 50$  nm) presented a very similar spectrum with slight modifications at the gap energy. ZnO nanoparticles exhibit also the reflectance decay at the bandgap, confirming that they retain the semiconductor character of ZnO. However, clear differences at the edge region are found with respect to the bulk and nanopowder ZnO samples. The nanoparticles show an increase in reflectance close to the edge ( $\sim 420$  nm) indicative of a different electronic structure at the bottom of the conduction band. In addition, the bandgap decay results sharper for the bulk and nanopowder while the nanoparticles exhibit a wider profile indicative of a more heterogeneous material and also a different density of available states. As it will be discussed later, the heterogeneity detected for the nanoparticles is in agreement with the formation of a layer at the particle surface. In addition, the bandgap profile depends on the capping molecule.

In the case of wurtzite ZnS, the energy gap is  $\sim 3.7$  [18], so different density of available states is present. Thiol samples, 5-12C-2, and NPs of the series-4 present, according to the XRD analysis (Sect. 2.2.1), a W-ZnS phase. As seen in Fig. 2.15, the edge region of those samples is displaced to lower wavelength, in agreement with the presence of a phase with a different density of states.

The photoluminescence spectra of the ZnO NPs are reported in Fig. 2.16. The emission spectra upon excitation with 320 nm light show a broad band centred at about 600 nm for the three samples. This emission is shifted with respect to the typical emission of bulk ZnO (centred at 550 nm) and its intensity depends on the capping molecule. This emission band is ascribed to an energy level induced by



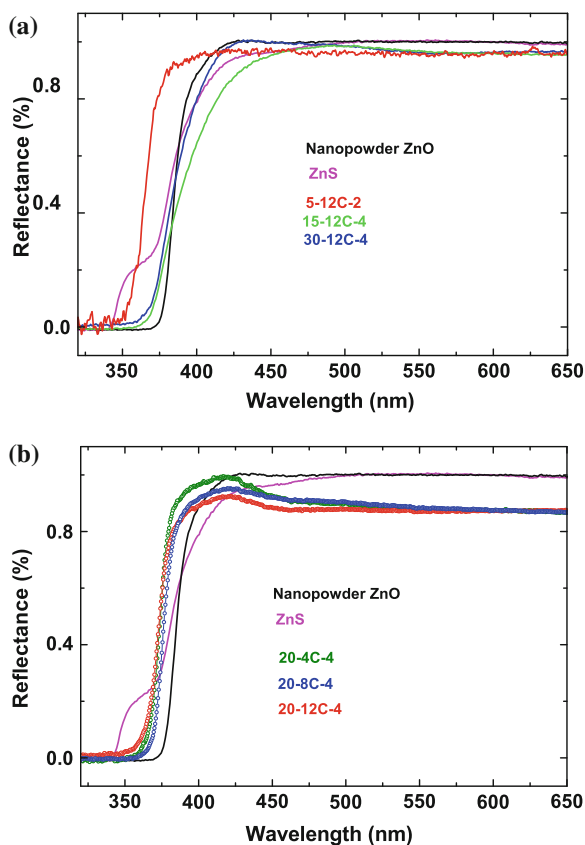
**Fig. 2.14** **a** Diffuse reflectance spectra for the series-1 of ZnO nanoparticles. Bulk and nanopowder ZnO references are also shown for comparison purposes. Curves are vertically displaced for clarity. **b** Detail of the band-gap profile



the presence of defects in ZnO. Although the particular defect responsible for the emission is still under discussion, it is commonly accepted that oxygen vacancies are involved [19].

The excitation spectra for the 570 nm emission exhibit a narrow peak at about 390 nm which correspond to the ZnO bandgap. The spectra show variations in intensity and a slight shifts depending on the capping molecule, peaking at 389 nm for THIOL, 397 nm for AMINE, and 390 for TOPO. The changes in the photoluminescence features are indicative of differences in the electronic configuration of the particle depending on the capping molecule. In particular, surface states are known to provide an alternative decay path for excited electrons; thus the changes in the PL intensity are associated with the presence and concentration of these surface states that will be determined by the bonds established between the ZnO particle and the capping molecule.

**Fig. 2.15** Diffuse reflectance spectra for the series-2 (a) and -4 (b) of ZnO nanoparticles. Bulk and nanopowder ZnO references are also shown for comparison purposes



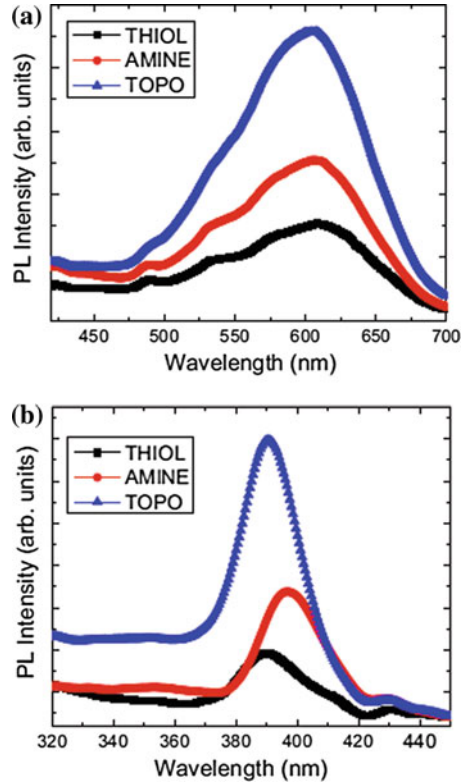
## 2.4 Magnetic Characterization: AC Susceptibility and Magnetization

The macroscopic magnetic measurements have been performed at the ICMM in collaboration with Dr. A. Espinosa and Dr. Mar García-Hernández. Magnetic measurements were performed using a Quantum Design superconducting quantum interference device (SQUID) magnetometer (Quantum Design MPMS-5S).

As discussed in the introductory chapter the reliability of the HTFM behaviour in DMSs and DMOs based on magnetization data centres a long-standing controversy. By this reason special care was taken during samples manipulation and handling. All possible sources of experimental errors, exhaustively reported in [20] were considered and avoided. Samples (always handled with nonmetallic tools) were placed into a gelatin capsule and mounted on straws. A gelatin capsule without any powder was also mounted on a straw and measured for control. Zn precursor (Zinc acetate dihydrate) was measured to detect contamination in the starting powder.



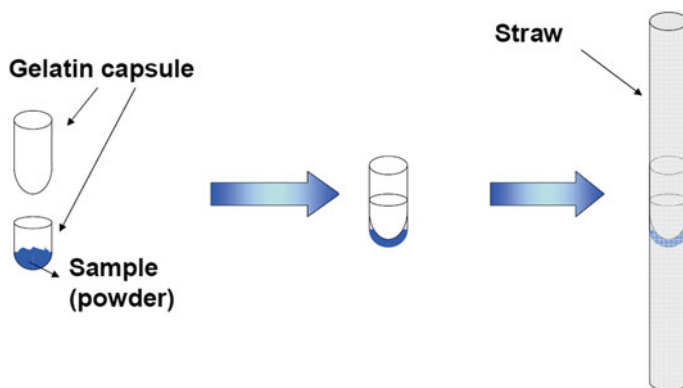
**Fig. 2.16** **a** Emission spectra upon excitation with 320 nm light. **b** Excitation spectra for the 570 nm emission



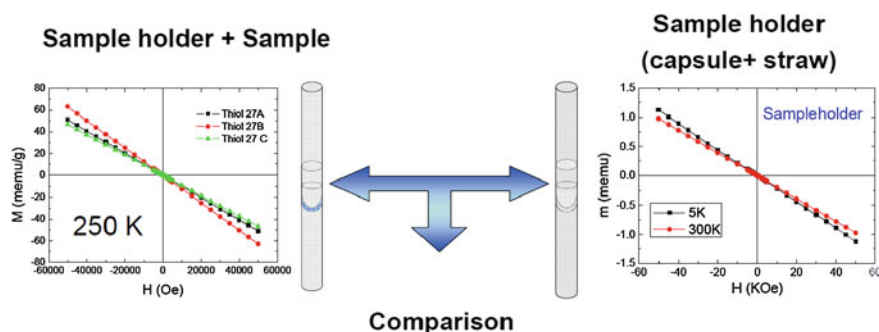
The measurements protocol is shown through Figs. 2.17 and 2.18. The samples are mounted on a straw as shown in 2.17. For all the samples magnetization vs applied magnetic field are recorded at low ( $T = 5$  K) and high temperatures ( $T = 250$  K or  $T = 300$  K). In addition, the temperature dependence of magnetization is also recorded. Samples are field cooled ( $H_{FC} = 5$  T) and the  $M(T)$  curve is recorded by applying a  $H_{mes} = 1000$  Oe magnetic field. Similar measurements are performed for the empty sample holder, and they are compared to those of the samples prior performing the mass normalization. For selected samples, several masses were measured in order to determine whether the magnetic signal scales with the mass.

Figure 2.19 summarizes the results of the SQUID measurements in the case of samples from the series-1. The same is shown in Fig. 2.20 for the sample holder.

Samples exhibit an overall diamagnetic behaviour at  $T = 5$  K (see panel a of Fig. 2.19). In addition, the thermal dependence of the magnetization (Fig. 2.19b) points out the existence of a paramagnetic signal following a Curie-Weiss law. By assuming that the paramagnetic susceptibility is negligible at 300 K, as the  $M(T)$  is flat at this temperature, the diamagnetic susceptibility is determined from the  $M(T)$  at high temperature. Then, by considering that the diamagnetic contribution is



**Fig. 2.17** Standard assembly of the sample: for measurements the sample is placed inside a gelatin capsule and mounted on a straw (No cotton, kapton or any other fixing materials are used)



**Fig. 2.18** The measurements are performed for the empty sample holder, in order to compare with the experimental results and remove any spurious signal

thermally independent the paramagnetic component at low temperature is determined from the difference in the low and high temperature susceptibility.

By subtracting a linear background to the  $M(H)$  curves (see panels c and d of Fig. 2.19) it is observed that the paramagnetic signal, recorded at 5 K, is negligible at high temperature, while a non-saturated ferromagnetic-like (FML) contribution is found. By FML behaviour we mean that the magnetization of the samples show most of the typical ferromagnetic characteristic, as remanence, coercivity and saturation.

As shown in Fig. 2.20 the magnetization curves of the sample holder used for the measurements exhibit a diamagnetic behaviour at both  $T = 5$  and 300 K. Moreover, the Curie-Weiss decay observed for the sample holder is 50 times smaller than for the THIOL sample. After subtracting a linear background the magnetization curves show also a FML component but it is at least five times smaller than that of any of the samples. In addition, this FML contribution strongly decays at high temperature being more than 20 times smaller at 300 K, while the observed decrease in the samples is

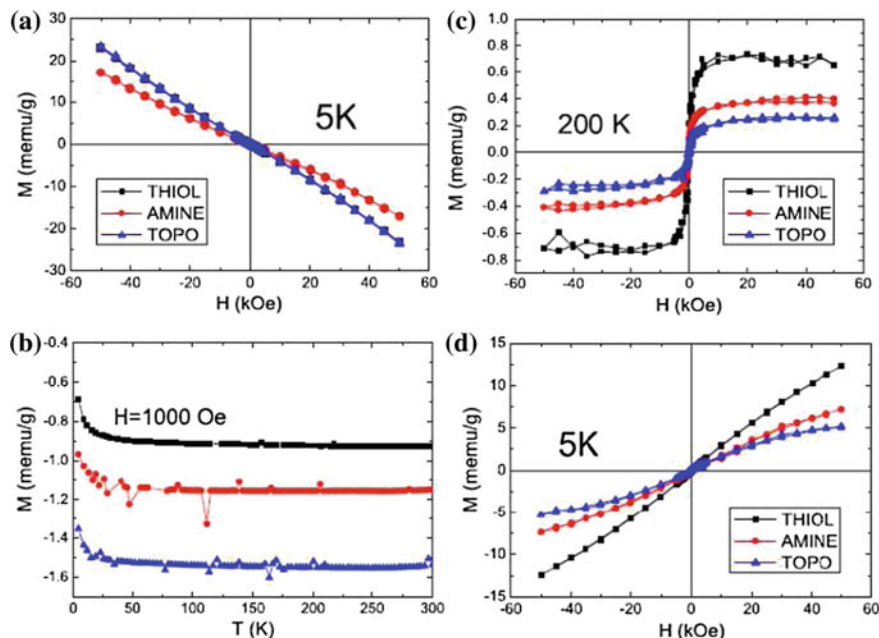


**Fig. 2.19** **a** Magnetization curves of TOPO, THIOL and AMINE. **b** Thermal dependence of the magnetization under an applied field of 1000 Oe. **c, d** Magnetization curves after subtracting the diamagnetic contribution, showing the paramagnetic and ferromagnetic components

significantly smaller (Fig. 2.19b). Finally, it should be noted that, when normalized to the mass (Fig. 2.20d), the FML components of the samples overlap indicating that this signal is not a background but it really arises from the sample. SQUID measurements on the precursor found no magnetic signal up to a resolution of  $5 \times 10^{-5}$  emu/g that is two orders of magnitude smaller than the FML signal reported here. The thermal dependence of the magnetization resulted different for each capping molecule, highlighting the influence of the surface bonds in this magnetism.

In the case of samples of series-I the FML contribution shows hysteresis ( $H_C \sim 200$  Oe) which remains also identical at high temperature. The value of the saturation magnetization,  $\sim 2$  memu/g, is in agreement with the values previously reported, although the dependence with the capping molecule is fairly different [21].

It is interesting at this point to compare the magnetic behaviour of the THIOL sample prior and after the calcination process. As shown in Fig. 2.21 despite both samples exhibit similar FML properties, the paramagnetic contribution is clearly reinforced in the calcinated sample. According to the XRD data, this seems related to the growth of ZnS-like regions upon calcination and the decrease of the amorphous phase. Therefore we can not rule out the importance of the structural conformation of the bonding region with the capping molecule into determining the magnetic properties of the samples.

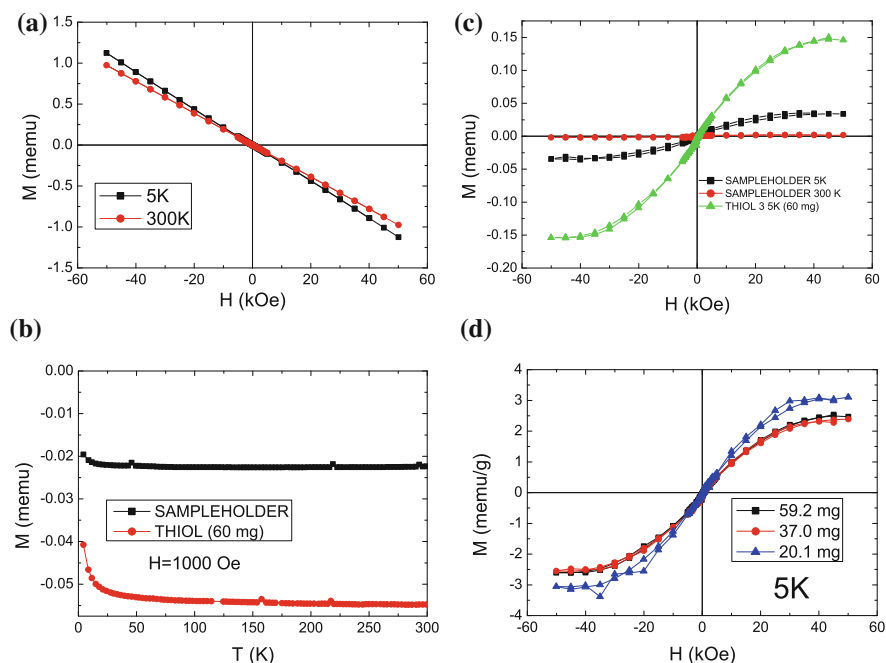
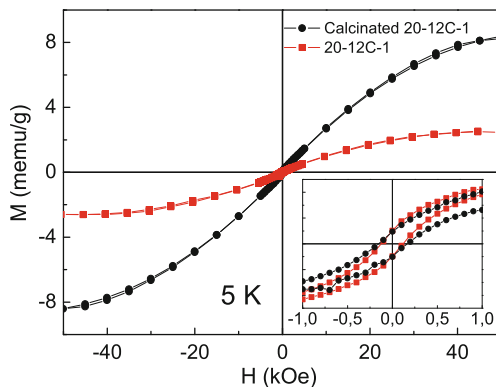


**Fig. 2.20** **a** Magnetization curves of the sample holder used for the measurements. **b** Thermal dependence of the magnetization (curve for THIOL sample is also presented for comparison purposes). **c** Magnetization curves after subtracting a linear background. **d** Ferromagnetic component for the THIOL sample at 5 K measured on three different specimens of 20, 40, and 60 mg

**Fig. 2.21** **a** Magnetization curves of the dodecanethiol-capped 20-12C-3 sample recorded at  $T = 5$  K prior and after the calcination. Detail of the low field region is given in lower inset



This behaviour is in agreement with the results found in the case of samples of series-2. The XRD patterns of the 15-12C-2 and 30-12C-2 samples (presented in Fig. 2.4) evidence a higher crystallinity of the ZnO component. As shown in Table 2.3 and Fig. 2.22, the decrease of the relative amount of the amorphous phase coincides

**Table 2.3** Coercivity and paramagnetic susceptibility ( $\chi_{PM}$ ) of series-1 and -2 (Thiol-capped NPs)

Sample	$\chi_{PM}$ (emu/g·Oe) (5 K)	$H_c$ (5 K) Oe	$H_c$ (250 K) Oe
20-12C-1	$2.00 \times 10^{-7}$	180	180
20-12C-1 Calcinated	$3.20 \times 10^{-7}$	250	200
5-12C-2	$1.98 \times 10^{-7}$	150	300
15-12C-2	$1.12 \times 10^{-7}$	250	200
30-12C-2	$8.30 \times 10^{-8}$	300	230

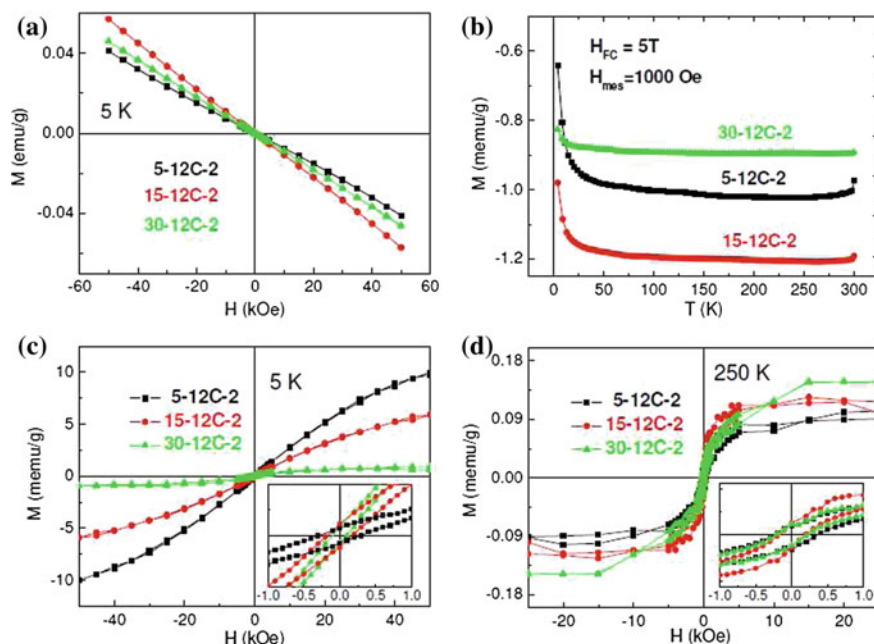


**Fig. 2.22** **a** Magnetization curves of the dodecanethiol-capped ZnO NPs (12C-2 series) measured at  $T = 5$  K. **b** Thermal dependence of the magnetization under an applied field of 1000 Oe. **c**  $T = 5$  K magnetization curves after subtracting the diamagnetic linear background (see text for details). In the *inset* a detail of the low field region, demonstrating the existence of remanence and hysteresis, is shown. **d** Same as panel **c** for  $T = 250$  K

with the decrease of the paramagnetic component. That is supported as well by the results of the series-5 samples (see Fig. 2.23).

It is important to note also that the occurrence of FML behaviour does not depend on the length of the organic molecule used for the capping. As a representative example of samples of series-4 we show in Fig. 2.24 the  $M(H)$  curves recorded for sample 20-4C-4, as well as the values of  $H_c$  in Table 2.4. Interestingly, despite coercivity is found, the FML/paramagnetic ratio found for these samples, showing the lowest crystallinity through the studied series, is the smallest within the synthesized series of NPs.

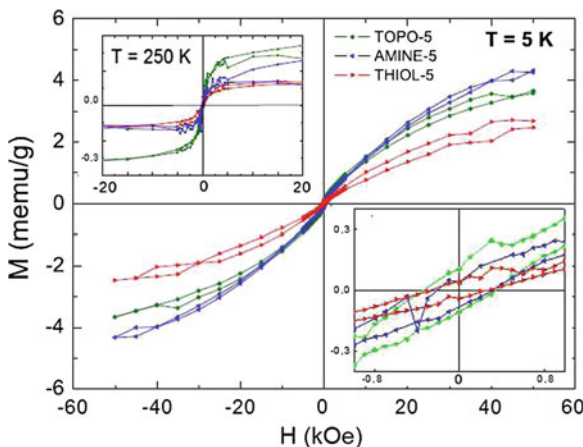


**Fig. 2.23** Magnetization curves of the series-5 TOPO, THIOL and AMINE-capped ZnO NPs measured at  $T = 5$  K. In the *inset* a detail of the low field region, demonstrating the existence of remanence and hysteresis, is shown. The *upper inset* show the magnetization curves at  $T = 250$  K

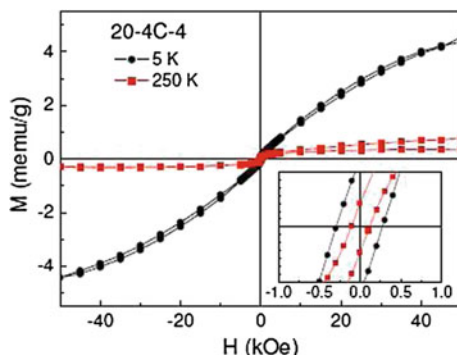


**Fig. 2.24** Magnetization curves of the butanethiol-capped 20-4C-4 sample measured at both  $T = 5$  K and  $T = 250$  K. Detail of the low field region is reported in the *inset*

These results suggest that amorphous phase enhances the paramagnetic contribution. Thus, an analogous study was carried out for thin films and ZnO/ZnS heterostructures, which present a high structural order. However, the comparison of  $M(H)$  curves (see Fig. 2.25) of the heterostructures with that of the ZnO monocrystal, indicates that the crystallinity does not explain the FML behaviour by itself. The ZnO monocrystal reference presents a pure paramagnetic behaviour at low temperature while the magnetic signal becomes nearly zero at room temperature. This could mean that the FML response should be somehow related to the modification of the original W-ZnO crystal structure.

To further consider that possibility a deeper study of the heterostructures is carried out. The FML contribution is maximized in the case of the  $(\text{ZnO}_{4\text{nm}}/\text{ZnS}_{4\text{nm}})_{10}$

**Table 2.4**  $H_c$  values determined for ZnO NPs of series-4

Sample	$H_c$ (Oe) T = 5 K	$H_c$ (Oe) T = 250 K
20-12C-4	150	150
20-12C-4	180	180
30-12C-4	300	230
20-4C-4	410	110
20-8C-4	—	150
20-12C-4	—	180
50-4C-4	—	100
50-8C-4	360	160
50-12C-4	310	140

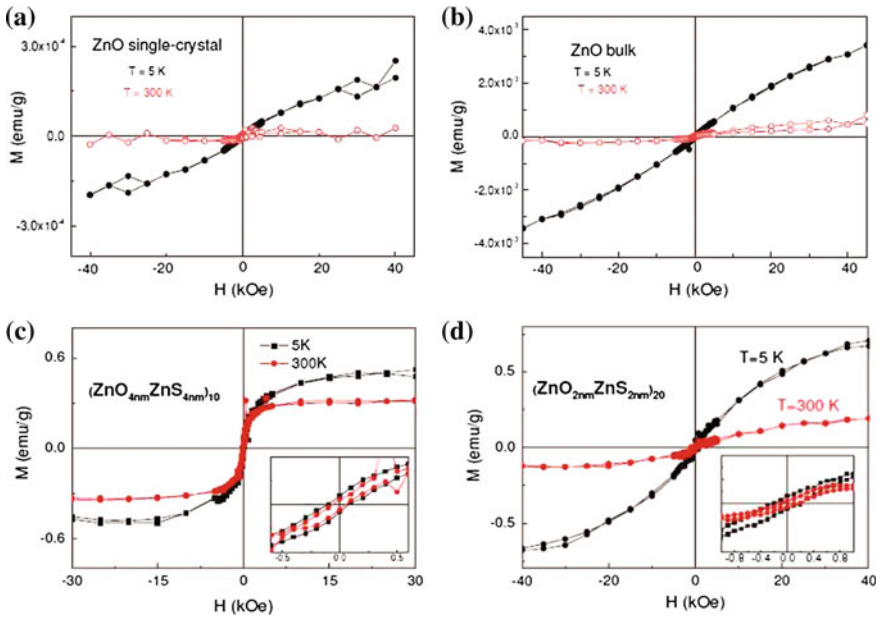
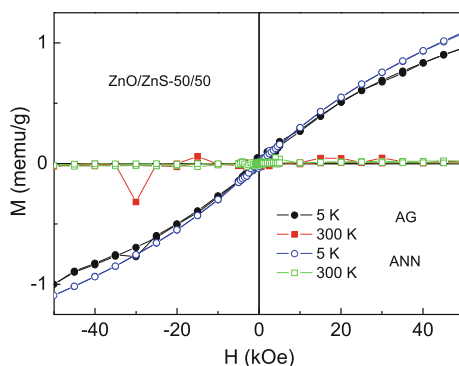


**Fig. 2.25** **a** Magnetization curves of a ZnO single crystal and **b** bulk ZnO measured at  $T = 5$  K and  $T = 300$  K. **c** Magnetization curves of the  $(\text{ZnO}_{4\text{nm}}/\text{ZnS}_{4\text{nm}})_{10}$  thin film measured at  $T = 5$  K and at room temperature. **d** Same as above in the case of the  $(\text{ZnO}_{2\text{nm}}/\text{ZnS}_{2\text{nm}})_{20}$  sample

heterostructure which shows this behaviour at both  $T = 5$  K and at room temperature (see Fig. 2.25). In contrast, the FML signal weakens for the  $(\text{ZnO}_{2\text{nm}}/\text{ZnS}_{2\text{nm}})_{20}$  sample, which presents larger mean interface roughness and what is more important, an average interface roughness of the order of the layer thickness.

These results point out that the FML component should be related to the development of pristine ZnO/ZnS interfaces. In order to test that, another ZnO/ZnS film was prepared by co-sputtering aiming to maximize the disorder and interpenetration at

**Fig. 2.26** Magnetization curves of the ZnS/ZnO-50/50 sample obtained by ZnS-ZnO co-sputtering: AG (as grown) and ANN (after annealing)



the ZnO/ZnS interfaces. As discussed in the previous section this sample shows an amorphous structure. As shown in Fig. 2.26 the FML is not observed in the sample obtained for co-sputtering, whose magnetization curves approach those obtained in the ZnO single crystal reference (see Fig. 2.26).

## References

1. L.L. Hench, J.K. West, *Chem. Rev.* **90**, 33 (1990)
2. C. Brinker, G. Scherer, *Sol-Gel Science: The Physics and Chemistry of Sol-Gel Processing* (Academic Pr. Inc., Boston, 1990)
3. L. Klein, *Sol Gel Optics: Processing and Applications* (Kluwer Academic Publisher, Berlin, 1994)
4. O. Lev, M. Tsionsky, L. Rabinovich, V. Glezer, S. Sampath, I. Pankratov, J. Gun, *Anal. Chem.* **67**, 22A (2012)
5. L. Klein, G. Garvey, *J. Non-Cryst. Solids* **38–39**, 45 (1980)
6. S. Sakka, K. Kamiya, *J. Non-Cryst. Solids* **48**, 31 (1982)
7. C. Brinker, *J. Non-Cryst. Solids* **100**, 31 (1988)
8. G. Whitesides, J. Mathias, C. Seto, *Science* **29**, 5036 (1991)
9. E. Céspedes, Ferromagnetism in wide band gap materials Mn-ZnO and Mn-Si<sub>3</sub>N<sub>4</sub> thin films, PhD Thesis, Universidad Autónoma de Madrid, 2009
10. W.R. Grove, *Philos. Trans. Roy. Soc. London* **142**, 87 (1852)
11. E. Goldstein, *Philos. Mag.* **15**, 372 (1908)
12. R. Parsons, *Thin Film Processes II. Part II-4: Sputter Deposition Processes* (Gulf Professional Publishing, Boston, 1991)
13. D. Smith, *Thin-Film Deposition: Principles and Practice* (McGraw Hill Professional, New York, 1995)
14. J.M. Albella, *Láminas delgadas y recubrimientos: preparación, propiedades y aplicaciones*, Biblioteca de Ciencias, CSIC (2003)
15. K. Zoerb, *Differential Sputtering Yields of Refractory Metals by Ion Bombardment at Normal and Oblique Incidences*, PhD Thesis, Colorado State University, 2006
16. N. Telling, S. Guilfoyle, D. Lovett, C. Tang, M. Crapper, M. Petty, *J. Phys. D: Appl. Phys.* **31**, 472 (1998)
17. J. Chaboy, R. Boada, C. Piquer, M.A. Laguna-Marco, M. García-Hernández, N. Carmona, J. Llopis, M.L. Ruíz-González, J. González-Calbet, J.F. Fernández, M.A. García, *Phys. Rev. B* **82**, 064411 (2010)



18. N. Üzar, M. Arikian, *Bull. Mater. Sci* **34**, 287 (2011)
19. A. van Dijken, E.A. Meulenkamp, D. Vanmaekelbergh, A. Meijerink, *J. Phys. Chem. B* **104**, 4355 (2000)
20. E. Fernández-Pinel, J. de La Venta, A. Quesada, M. García, *J. Appl. Phys.* **105**, 1 (2009)
21. M.A. García, J.M. Merino, E. Fernández-Pinel, A. Quesada, J. de La Venta, M.L. González, G.R. Castro, P. Crespo, J. Llopis, J.M. González-Calbet, A. Hernando, *Nano Lett.* **7**, 1489 (2007)

Relationship Between Structure and Magnetic  
Behaviour in ZnO-Based Systems

Guglieri, C.

2015, XIV, 146 p. 104 illus., 52 illus. in color., Hardcover

ISBN: 978-3-319-18886-7